



UNIVERSITY OF LEEDS

This is a repository copy of *Di-Iron(II) [2+2] Helicates of Bis-(Dipyrazolylpyridine) Ligands – the Influence of the Ligand Linker Group on Spin State Properties.*

White Rose Research Online URL for this paper:

<https://eprints.whiterose.ac.uk/193454/>

Version: Accepted Version

Article:

Kulmaczewski, R orcid.org/0000-0002-3855-4530, Armstrong, IT, Catchpole, P orcid.org/0000-0003-3048-060X et al. (5 more authors) (2023) Di-Iron(II) [2+2] Helicates of Bis-(Dipyrazolylpyridine) Ligands – the Influence of the Ligand Linker Group on Spin State Properties. *Chemistry: A European Journal*, 29 (9). e202202578. ISSN 0947-6539

<https://doi.org/10.1002/chem.202202578>

This is an author produced version of a paper published in *Chemistry: A European Journal*. Uploaded in accordance with the publisher's self-archiving policy. This article may be used for non-commercial purposes in accordance with the Wiley Terms and Conditions for Self-Archiving.

Reuse

Items deposited in White Rose Research Online are protected by copyright, with all rights reserved unless indicated otherwise. They may be downloaded and/or printed for private study, or other acts as permitted by national copyright laws. The publisher or other rights holders may allow further reproduction and re-use of the full text version. This is indicated by the licence information on the White Rose Research Online record for the item.

Takedown

If you consider content in White Rose Research Online to be in breach of UK law, please notify us by emailing eprints@whiterose.ac.uk including the URL of the record and the reason for the withdrawal request.



eprints@whiterose.ac.uk
<https://eprints.whiterose.ac.uk/>

Di-Iron(II) [2+2] Helicates of Bis-(Dipyrzoly)pyridine) Ligands – the Influence of the Ligand Linker Group on Spin State Properties

Rafal Kulmaczewski,^[a] Isaac T. Armstrong⁺,^[a] Pip Catchpole⁺,^[a,b] Emily S. J. Ratcliffe⁺,^[a] Hari Babu Vasili,^[c] Stuart L. Warriner,^[a] Oscar Cespedes,^[c] and Malcolm A. Halcrow^{*[a]}

[a] Dr. R. Kulmaczewski, I. Armstrong, P. Catchpole, E. S. J. Ratcliffe, Dr. S. L. Warriner, Prof M A. Halcrow
School of Chemistry, University of Leeds, Woodhouse Lane, Leeds LS2 9JT, UK.
E-mail: m.a.halcrow@leeds.ac.uk.

Homepage: <https://eps.leeds.ac.uk/chemistry/staff/4173/professor-malcolm-halcrow>

[b] Current address: Department of Chemistry, Lancaster University, Lancaster LA1 4YB, UK.

[c] Dr. H. B. Vasili, Dr. O. Cespedes

School of Physics and Astronomy, W. H. Bragg Building, University of Leeds, Leeds LS2 9JT, UK.

[+] These authors contributed equally to this manuscript.

Supporting information for this article is given via a link at the end of the document.

Abstract: Four *bis*[2-(pyrazol-1-yl)-6-(pyrazol-3-yl)pyridine] ligands have been synthesized, with butane-1,4-diyl (L^1), pyrid-2,6-diyl (L^2), benzene-1,2-dimethylenyl (L^3) and propane-1,3-diyl (L^4) linkers between the tridentate metal-binding domains. L^1 and L^2 form $[\text{Fe}_2(\mu-L)_2]X_4$ ($X^- = \text{BF}_4^-$ or ClO_4^-) helicate complexes when treated with the appropriate iron(II) precursor. Solvate crystals of $[\text{Fe}_2(\mu-L^1)_2][\text{BF}_4]_4$ exhibit three different helicate conformations, which differ in the torsions of their butanediyl linker groups. The solvates exhibit gradual thermal spin-crossover, with examples of stepwise switching and partial spin-crossover to a low temperature mixed-spin form. Salts of $[\text{Fe}_2(\mu-L^2)_2]^{4+}$ are high-spin, which reflects their highly twisted iron coordination geometry. The composition and dynamics of assembly structures formed by iron(II) with L^1 - L^3 vary with the ligand linker group, by mass spectrometry and ^1H NMR. Gas phase DFT calculations imply the butanediyl linker conformation in $[\text{Fe}_2(\mu-L^1)_2]^{4+}$ influences its spin state properties, but show anomalies attributed to intramolecular electrostatic repulsion between the iron atoms.

Introduction

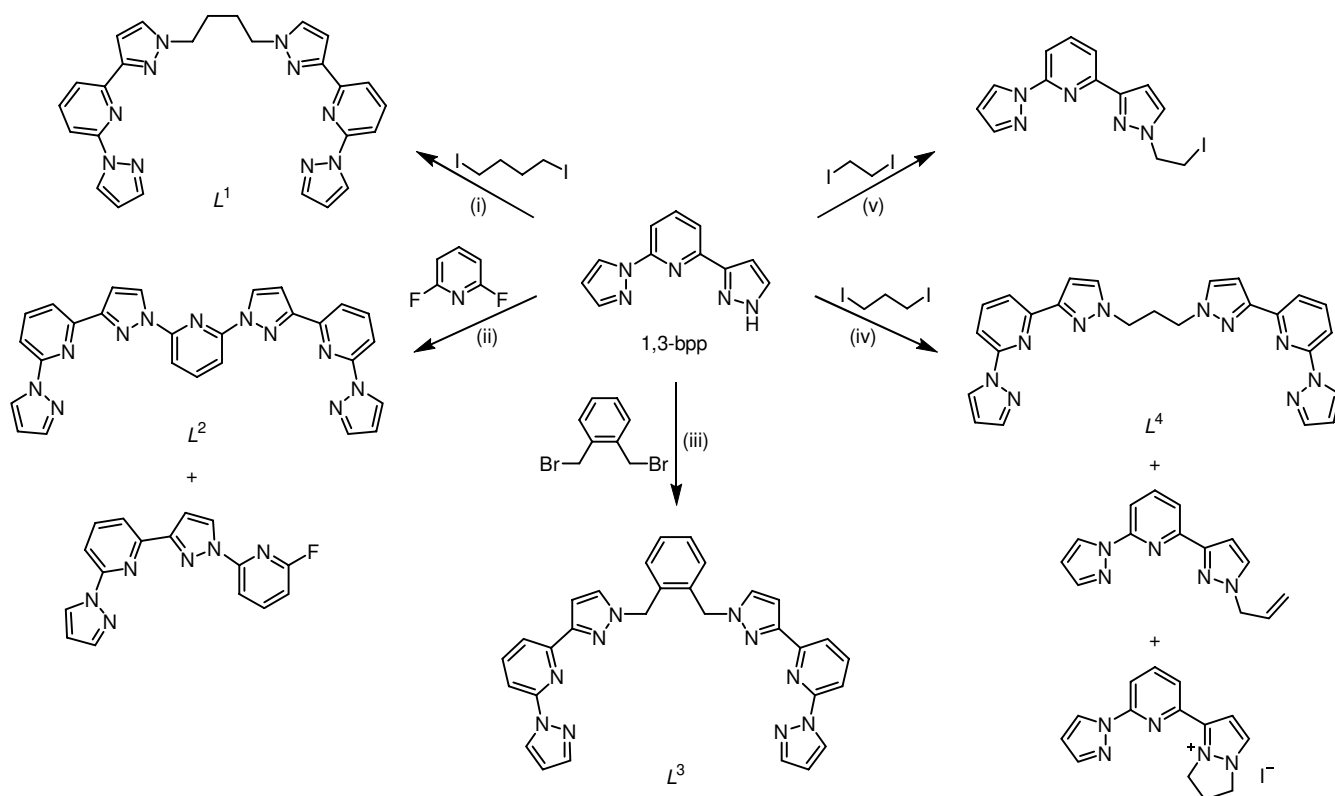
Spin-crossover (SCO) compounds are versatile molecular switches, where a transition ion undergoes a change in spin state under heating/cooling, hydrostatic pressure, visible light irradiation or another physical stimulus.^[1-4] An SCO transition influences several bulk properties of a solid material,^[2,5] which has been harnessed in the laboratory for macroscopic^[6] and nanoscale^[7] applications including SCO compounds as switching components. Supramolecular assemblies of multiple SCO centers afford spatially defined arrays of SCO sites, which may switch independently or in concert depending on their topology and structural rigidity.^[8,9] Moreover, some assembly structures can modulate their spin states by encapsulating guest molecules,^[10-12] or through other supramolecular interactions.^[13] Molecular squares or grids,^[8,9,14,15] tetrahedral^[8,10,16-18] and cubane^[9,11,19,20] cage complexes with SCO-active vertices are well-established, while other SCO cluster and cage architectures have also been reported.^[9,21-27] However, the best-developed class of SCO supramolecular assembly is also one of the simplest, namely helicate complexes.^[8,16]

The first dinuclear SCO helicates were reported by Piguet *et al*, who combined SCO iron(II) centers and emissive lanthanide ions to produce switchable, emissive molecular constructs based on [3+3]-helicate scaffolds.^[28] More recently, ditopic *bis*-bidentate Schiff bases^[16,17,29,30] or *bis*-diheterocyclic ligands^[11-13,31] have been versatile scaffolds for di-iron(II) [3+3]-helicates, which often exhibit thermal SCO. Using longer spacers between the metal-binding domains in these ligands affords helicates with internal cavities, which can encapsulate anion guests. The guest species influence the temperature and completeness of SCO, with larger guests disfavoring the low-spin state on steric grounds.^[12]

All these examples are [3+3]-helicate assemblies, with three *bis*-bidentate ligands wrapped around six-coordinate metal centers. SCO in diiron(II) [3+3]-helicate complexes usually occurs gradually with temperature, and is often ill-defined and incomplete. Conversely, there is just one prior example of a diiron(II) [2+2]-helicate complex supported by a *bis*-tridentate ligand scaffold, whose salts exhibit abrupt and hysteretic spin-transitions in the solid state.^[32] Such cooperative switching properties are more useful for the applications listed above.

Some of the most widely studied SCO complexes are derived from $[\text{Fe}(\text{bpp})_2]^{2+}$ salts (bpp = 2,6-di(pyrazolyl)pyridine). Three isomers of the bpp ligand are available: 2,6-di(pyrazol-1-yl)pyridine (1-bpp),^[33-36] 2,6-di(1*H*-pyrazol-3-yl)pyridine (3-bpp),^[37,38] and the unsymmetric 2-(pyrazol-1-yl)-6-(1*H*-pyrazol-3-yl)pyridine (1,3-bpp).^[34,39-41] Hundreds of iron(II) complex salts supported by bpp derivatives are known, many of which exhibit SCO at accessible temperatures.^[33-41]

As a continuation of our long-standing interest in $[\text{Fe}(\text{bpp})_2]^{2+}$ chemistry,^[33-35] we now report an investigation of ditopic ligands containing two 1,3-bpp domains linked by different spacers (Scheme 1).^[42-44] Some of these cleanly yielded dinuclear iron(II) helicate complexes. Different crystals of one complex adopt one of three helical conformations, which differ in the torsions of the ligand linker and show distinct spin state behaviors. DFT calculations investigating the influence of the linker conformation on the complex spin state are also described, which highlight unexpected challenges in computing the spin states of multinuclear complexes.



Scheme 1. The ligand synthesis reactions undertaken in this work. Reagents and conditions: Reagents and conditions: (i) NaH, thf, 298 K then 0.5 eq 1,4-diiodobutane, reflux, 72 hrs; (ii) NaH, dmf, 298 K then 0.5 eq 2,6-difluoro-

pyridine, reflux, 24 hrs; (iii) NaH, thf, 298 K then 0.5 eq 1,2-bis(bromomethyl)-benzene, reflux, 72 hrs; NaH, thf, 298 K then 0.5 eq 1,3-diiodopropane, reflux, 24 hrs; (v) NaH, diglyme then 0.5 equiv 1,2-diiodoethane, 130 °C, 2-14 days.

Results and Discussion

Deprotonation of 1,3-bpp^[39] in dry tetrahydrofuran (thf) or *N,N*-dimethylformamide (dmf), then addition of 0.5 equiv 1,4-diiodobutane, 2,6-difluoropyridine or 1,2-bis(bromomethyl)benzene, yields 1,4-bis(3-{2-[pyrazol-1-yl]pyrid-6-yl}pyrazol-1-yl)butane (L¹), 2,6-bis(3-{2-[pyrazol-1-yl]pyrid-6-yl}pyrazol-1-yl)pyridine (L²) and 1,2-bis-(3-{2-[pyrazol-1-yl]pyrid-6-yl}pyrazol-1-ylmethyl)benzene (L³) after 1-3 days under heating (Scheme 1). While L¹ and L³ were obtained in high yields in NMR purity, L² was always contaminated by its monosubstituted byproduct as shown in Scheme 1. Their poor solubility made it impossible to separate the two compounds. However the mixture still afforded analytically pure iron(II)/L² complexes when treated with iron salts, as described below.

Attempts to prepare analogues of L¹ with shorter alkyl linker groups were less successful. The desired 1,3-bis(3-{2-[pyrazol-1-yl]pyrid-6-yl}pyrazol-1-yl)propane (L⁴, Scheme 1) was obtained by this route by using 1,3-diiodopropane as starting material, but in inconsistent lower yields. Two significant byproducts of this reaction were identified, which are both derived from monosubstituted (3-iodopropyl)-1,3-bpp (Scheme 1). The same process using 1,2-diiodoethane gave monosubstituted (2-iodoethyl)-1,3-bpp as the only isolable product, even after two weeks of reaction at higher temperatures in diglyme (Scheme 1). Hence, double substitution of α,ω -diiodoalkanes by 2 equiv 1,3-bpp is apparently sluggish for short chain lengths, and the butaned-yl group in L¹ was the shortest alkyl linker that was successfully used in this study.

Treatment of L¹ or L² with 1 equiv FeX₂·6H₂O (X⁻ = BF₄⁻ or ClO₄⁻) in nitromethane afforded orange-brown (for L¹) or bright yellow (L²) solids after the usual workup. The complexes were identified as dinuclear helicates, [Fe₂(μ -L)₂]X₄ (L = L¹, **1X₄**; L = L², **2X₄**) by X-ray crystallography, microanalysis, mass spectrometry and ¹H NMR. Analogous complexations using L³ yielded glassy orange/yellow solids of uncertain composition, which are described in more detail below. No analytically pure complex of L⁴ was obtained during this study.

The salt **1[BF₄]₄** was crystallized from three different solvents using diethyl ether as antisolvent. Crystals grown from acetonitrile (**1[BF₄]₄·2MeCN·Et₂O**) or acetone (**1[BF₄]₄·*n*Me₂CO**, *n* ≈ 2.5) were visually homogeneous. However, recrystallization of **1[BF₄]₄** from MeNO₂/Et₂O affords two pseudopolymorphs with needle (**1[BF₄]₄·*m*MeNO₂**, *m* ≈ 4.5) and prismatic (**1[BF₄]₄·2MeNO₂**) morphologies. All these solvates were crystallographically characterized, although the refinement of **1[BF₄]₄·*m*MeNO₂** is highly disordered and less precise than for the other crystals.

Three helicate conformations are observed in the four structures, which differ in the torsions of their butaned-yl linker groups. In **1[BF₄]₄·2MeNO₂** [Figure 1, molecule (a)] both butaned-yl linkers have two *gauche* torsions. Both its iron atoms are low-spin at the temperature of measurement (125 K; Table 1). In contrast, **1[BF₄]₄·2MeCN·Et₂O** [molecule (c)] has just one *gauche* torsion at each butaned-yl group. One iron atom in that crystal is high-spin and the other is low-spin at 125 K. The complex in **1[BF₄]₄·*m*MeNO₂** also adopts conformation (c), and is predominantly high-spin at that temperature (Figure S17, Table 1). Lastly, the helicate in **1[BF₄]₄·*n*Me₂CO** [molecule (b)] contains

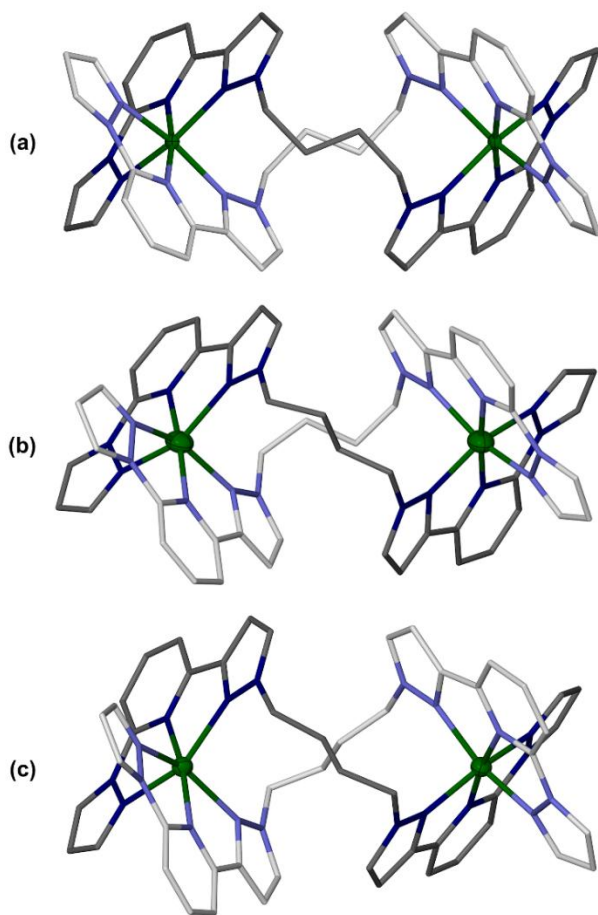


Figure 1. The conformations adopted by $[\text{Fe}_2(\mu\text{-}L^1)_2]^{4+}$ in: (a) $1[\text{BF}_4]_4 \cdot 2\text{MeNO}_2$; (b) $1[\text{BF}_4]_4 \cdot n\text{Me}_2\text{CO}$; and (c) $1[\text{BF}_4]_4 \cdot 2\text{MeCN} \cdot \text{Et}_2\text{O}$. The L^1 ligands in each molecule are distinguished with pale and dark coloration, and H atoms are omitted for clarity. The crystallographic view of molecule (a) has been inverted, to give it the same handedness as the other molecules in the Figure. Color code: C, white or gray; N, pale or dark blue; Fe, green.

one of each butanediyl group conformation, and was measured at two temperatures. Both its iron atoms are high-spin at 250 K. However, at 100 K Fe(1) adopts a mixed high/low-spin population, while Fe(2) has become fully low-spin (Table 1). Hence, the two iron centers in $1[\text{BF}_4]_4 \cdot n\text{Me}_2\text{CO}$ evidently undergo SCO at different temperatures on cooling.

The relative orientations of the two $[\text{Fe}(\text{bpp})_2]^{2+}$ domains are quite similar in all these helicate conformations (Figure 1). However, each additional butanediyl *gauche* torsion pushes the two iron atoms further apart, by 0.3-0.4 Å (Table 1). The two solvates adopting conformation (c) exhibit almost identical Fe...Fe distances, implying this parameter may be only slightly perturbed by crystal packing effects. SCO in $1[\text{BF}_4]_4 \cdot n\text{Me}_2\text{CO}$ also has little effect on its Fe...Fe separation (Table 1).

The metric parameters at the iron centers in the $1[\text{BF}_4]_4$ solvates are mostly typical for SCO-active $[\text{Fe}(\text{bpp})_2]^{2+}$ derivatives (Table 1).^[33-41] An exception is Fe(1) in $1[\text{BF}_4]_4 \cdot 2\text{MeCN} \cdot \text{Et}_2\text{O}$, which is high-spin at 125 K with a more distorted coordination geometry. This is described by two parameters: the *trans*-N{pyridyl}-Fe-N{pyridyl} angle (ϕ), which is 167.9(3)°; and, the least squares planes of the two bpp moieties bound to each metal atom (θ), which is 73.87(7)°.^[45,46] An undistorted metal center of this type would have $\phi = 180$ and $\theta = 90$ °. Crystalline, high-spin $[\text{Fe}(\text{bpp})_2]^{2+}$ derivatives with comparable distortions to Fe(1) rarely exhibit thermal SCO,^[47] and are kinetically trapped in their high-spin form upon cooling.^[48] Hence, the distorted geometry at Fe(1) may explain the incomplete SCO in $1[\text{BF}_4]_4 \cdot 2\text{MeCN} \cdot \text{Et}_2\text{O}$ (Figure 2). The other iron atom in that structure, Fe(2), is low-spin at the temperature of measurement and adopts a more regular coordination geometry, as expected.

The polycrystalline $1[\text{BF}_4]_4$ solvatomorphs decompose to powders when exposed to air, leading to significant structural changes or loss of crystallinity by powder diffraction (Figures S20-S22). Elemental analysis implies some lattice solvent is retained,

Table 1. Structural parameters from the crystal structures of $1[\text{BF}_4]_4$.^[6] The conformations listed refer to those in Figure 1.

	$1[\text{BF}_4]_4 \cdot 2\text{MeNO}_2$	$1[\text{BF}_4]_4 \cdot n\text{Me}_2\text{CO}$	$1[\text{BF}_4]_4 \cdot 2\text{MeCN} \cdot \text{Et}_2\text{O}$	$1[\text{BF}_4]_4 \cdot m\text{MeNO}_2$ ^[b]
Conformation	(a)	(b)	(c)	(c)
T [K]	125	250	100	125
V_{oh} {Fe(1), Fe(2)} [\AA^3]	9.649(13), 9.651(12)	12.318(10), 12.249(10)	11.231(14), 9.965(12)	12.19(3), 9.92(2)
Fe...Fe [\AA]	8.5452(11)	8.1477(6)	8.1221(9)	7.8570(18)
Σ {Fe(1), Fe(2)} [°]	88.9(5), 87.7(6)	141.2(3), 139.8(4)	125.7(6), 97.1(5)	157(1), 89(1)
Θ {Fe(1), Fe(2)} [°]	295, 290	466, 458	483, 313	493, 295
ϕ {Fe(1), Fe(2)} [°]	171.8(2), 174.1(2)	168.53(10), 173.69(11)	171.54(14), 175.52(16)	167.9(3), 173.4(3)
θ {Fe(1), Fe(2)} [°]	87.66(3), 84.28(3)	85.96(3), 83.62(3)	85.43(4), 84.30(4)	73.87(7), 84.22(7)
				79.46(10)/81.08(9), 79.65(11)/80.42(12)

[a] V_{oh} , Σ , and Θ are indices characteristic for the spin state of a complex,^[49] while ϕ and θ are defined in the text and relate to structural distortions found in $[\text{Fe}(\text{bpp})_2]^{2+}$ derivatives.^[45,46] [b] There is pyrazolyl group disorder in this crystal structure, and values for both ligand disorder sites are given for each iron atom.

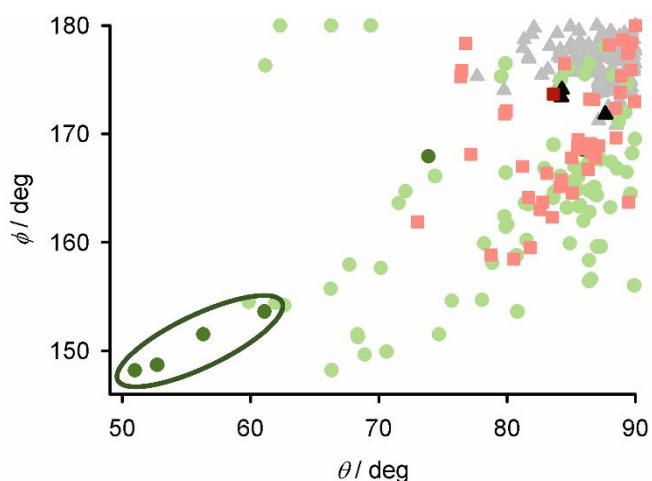


Figure 2. Published distortion parameters for $[\text{Fe}(\text{1-bpp})_2]^{2+}$ complexes which are low-spin (gray triangles); high-spin and SCO-active (red squares); and which remain high-spin on cooling (green circles).^[33-36] The iron centers in $1[\text{BF}_4]_4$ and $2[\text{ClO}_4]_4$ (Tables 1 and 2) are plotted using the same symbols in dark coloration, with data from the structures of $2[\text{ClO}_4]_4$ being circled.

or replaced by atmospheric moisture, in the air-dried solids. Magnetic susceptibility data show the materials undergo gradual thermal SCO, although each is different in form (Figure 3). All the magnetic data are reversible in cooling and warming temperature ramps, and so are not affected by *in situ* solvent loss. While no single crystals of $1[\text{ClO}_4]_4$ were achieved, samples of that salt obtained from the same solvents show comparable X-ray powder patterns and SCO profiles to their BF_4^- analogues (Figures S23-S25).

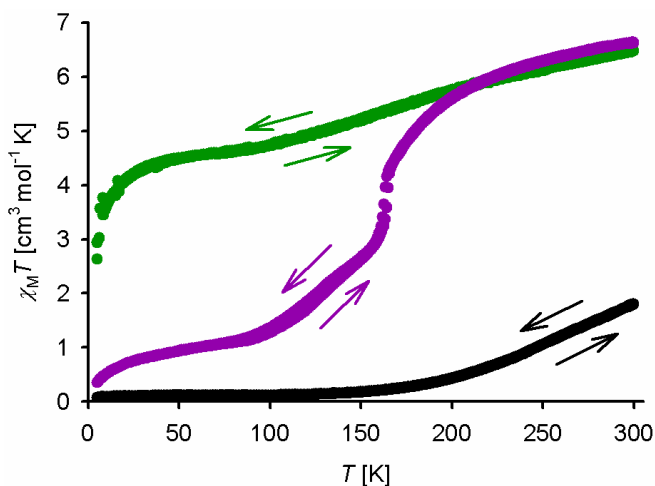


Figure 3. Variable temperature magnetic susceptibility data for dried polycrystalline samples of: $1[\text{BF}_4]_4 \cdot m\text{MeNO}_2$ (black); $1[\text{BF}_4]_4 \cdot n\text{Me}_2\text{CO}$ (purple); and $1[\text{BF}_4]_4 \cdot 2\text{MeCN} \cdot \text{Et}_2\text{O}$ (green). All data were measured on a 300-5-300 K temperature ramp, at scan rate 5 K min^{-1} .

Most interestingly, air-dried $1[\text{BF}_4]_4 \cdot n\text{Me}_2\text{CO}$ is high-spin at 300 K and undergoes stepwise SCO on cooling, with an abrupt discontinuity near 160 K corresponding to 50 % conversion. That is consistent with the crystallographic observation that the two iron sites in that material undergo SCO at different temperatures. The transition is *ca* 80 % complete at 100 K in the magnetic data, but shows a residual paramagnetism below that temperature. That

implies kinetic trapping of the remaining material in its high-spin state below 100 K,^[50] which is often observed in $[\text{Fe}(\text{bpp})_2]^{2+}$ derivatives whose SCO extends to such low temperature.^[47,51]

A mixture of the nitromethane solvates of $1[\text{BF}_4]_4 \cdot m\text{MeNO}_2$ undergoes significant structural changes during air-drying by powder diffraction. The material is low-spin below 100 K, and shows a very gradual continuous SCO above that temperature such that *ca* 30 % of its iron atoms are high-spin at 300 K (Figure 3). Interestingly, that is more consistent with the crystal structure of the minor solvatomorph $1[\text{BF}_4]_4 \cdot 2\text{MeNO}_2$, which is low-spin at 125 K, than with the major crystal form $1[\text{BF}_4]_4 \cdot m\text{MeNO}_2$. Conversely, air-dried $1[\text{BF}_4]_4 \cdot 2\text{MeCN} \cdot \text{Et}_2\text{O}$ is poorly crystalline and is high-spin at room temperature, showing a gradual SCO on cooling which is *ca* 30 % complete at 100 K.

Full structure analyses were obtained from solvent-free $2[\text{ClO}_4]_4$, and a solvate crystal $2[\text{ClO}_4]_4 \cdot 3\text{MeNO}_2 \cdot 0.75\text{H}_2\text{O}$. The $[\text{Fe}_2(\mu\text{-}L^2)_2]^{4+}$ helicate has the same ligand conformation in both crystals, with the iron atoms being bound by the two L^2 ligands in the expected *bis*-tridentate fashion (Figure 4). While crystals of $2[\text{BF}_4]_4$ diffracted X-rays more weakly, a partial refinement from a nitromethane solvate of that salt confirmed it has the same connectivity as the perchlorate crystals (Figure S28). The metal ions are high-spin from their metric parameters, and adopt highly twisted coordination geometries with $148.18(9) \leq \phi \leq 153.60(9)^\circ$ and $50.96(3) \leq \theta \leq 61.08(2)^\circ$ (Table 2).^[45] These include the most severe θ distortions yet reported for a $[\text{Fe}(\text{bpp})_2]^{2+}$ derivative,^[46] which probably reflects the steric constraints of the rigid L^2 ligands. Interestingly, ϕ and θ follow an almost linear relationship in these two crystals, implying the iron atoms in $[\text{Fe}_2(\mu\text{-}L^2)_2]^{4+}$ consistently follow the same structural distortion pathway (Figure 2).

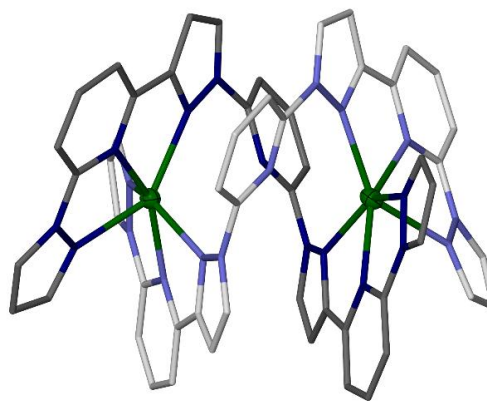


Figure 4. The $[\text{Fe}_2(\mu\text{-}L^2)_2]^{4+}$ helicate in the crystal structure of $2[\text{ClO}_4]_4$. Details as for Figure 1.

The N atom of the central pyridyl ring of each ligand is oriented towards an open face of an iron atom, but at a distance of $\text{Fe} \cdots \text{N} = 3.1\text{-}3.2 \text{ \AA}$ which is too long for a significant covalent interaction. This coordination geometry implies the 2X_4 salts should remain high-spin on cooling (Figure 2), which was confirmed by magnetic measurements (Figure S32).

The helicate structure in $[\text{Fe}_2(\mu\text{-}L^2)_2]^{4+}$ is further stabilized by one short and two longer intramolecular $\pi \cdots \pi$ interactions, between aromatic residues on each ligand (Figures S29-S30, Table S6).

Table 2. Structural parameters from the crystal structures of **2[ClO₄]₄**. Details as for Table 1.

	2[ClO₄]₄	2[ClO₄]₄·3MeNO₂·0.75H₂O
$V_{\text{oh}} \{ \text{Fe}(1), \text{Fe}(2) \} [\text{\AA}^3]$	11.912(9), 11.496(9)	11.642(9), 11.658(9)
$\text{Fe} \cdots \text{Fe} [\text{\AA}]$	5.1401(6)	5.1906(6)
$\Sigma \{ \text{Fe}(1), \text{Fe}(2) \} [^\circ]$	225.4(3), 213.0(3)	216.7(3), 205.6(3)
$\Theta \{ \text{Fe}(1), \text{Fe}(2) \} [^\circ]$	466, 459	464, 584
$\varphi \{ \text{Fe}(1), \text{Fe}(2) \} [^\circ]$	148.68(10), 151.50(9)	148.18(9), 153.60(9)
$\theta \{ \text{Fe}(1), \text{Fe}(2) \} [^\circ]$	52.71(5), 56.30(4)	50.96(3), 61.08(2)

An additional intermolecular $\pi \cdots \pi$ interaction in both crystals associates the helicite cations into centrosymmetric dimers (the crystals are racemic, containing equal numbers of Λ and Δ helical molecules in their asymmetric unit).

Reaction of L^3 with 1 equiv of the same iron(II) salts yielded glassy orange solids, which were perfectly amorphous by powder diffraction. These solids analyzed reasonably to the empirical formulae $[\text{Fe}(L^3)]X_2$ (**3X₂**; $X^- = \text{BF}_4^-$ or ClO_4^-), with some included lattice solvent. The amorphous materials are essentially high-spin at room temperature, and show very gradual SCO equilibria on cooling in ca 15 % of their iron centers (Figures S33-S34).

Electrospray mass spectra of **1[ClO₄]₂**, **2[ClO₄]₂** and **3[ClO₄]₂** from MeCN solution are superficially similar, with an intense peak assigned to $[\text{FeL}(\text{ClO}_4)]^+$ ($L = L^1$ - L^3) and one principal peak at higher mass ($L = L^1$, $m/z = 1363.1526$; $L = L^2$, $m/z = 1405.0681$; $L = L^3$, $m/z = 1459.1513$). Unexpectedly however, simulations of those dication peaks reveal they arise from a combination of $[\text{Fe}_2L_2(\text{ClO}_4)_3]^+$, $[\text{Fe}_4L_4(\text{ClO}_4)_6]^{2+}$ and, for **1[ClO₄]₂**, $[\text{Fe}_6(L^1)_6(\text{ClO}_4)_9]^{3+}$ species (Figures 5, S36 and S37).^[52,53] Weak higher mass peaks from pentameric and hexameric assemblies are also visible for **3[ClO₄]₂**. Hence, solutions of all three complexes are a mixture of assembly structures under these conditions. The spectrum of **1[ClO₄]₂** shows more fragmentation than the other complexes, including metal-free L^1 which is not present in the other spectra. That is consistent with the higher lability of **1[ClO₄]₂** observed by NMR (see below).

The ^1H NMR of **1[ClO₄]₂** in CD_3CN shows just one paramagnetic, C_2 -symmetric L^1 environment (Figure S38). The butanediyl CH_2 groups are diastereotopic in the spectrum, which is consistent with the chirality of the helicite structure. In contrast the ^1H NMR of **2[ClO₄]₂** in CD_3CN contains one principal C_2 -symmetric L^2 environment, but with a second paramagnetic L^2 -containing species comprising 10-15 % of the sample by integration (Figure S39). Neither spectrum has peaks in the diamagnetic region from uncoordinated ligand, or to dangling bpp residues from mono-coordinated L^1 or L^2 . These data imply interconversion of the assembly structures detected by mass spectrometry occurs rapidly in solution when $L = L^1$, giving a time-averaged NMR spectrum, but is slower than the NMR timescale when $L = L^2$.

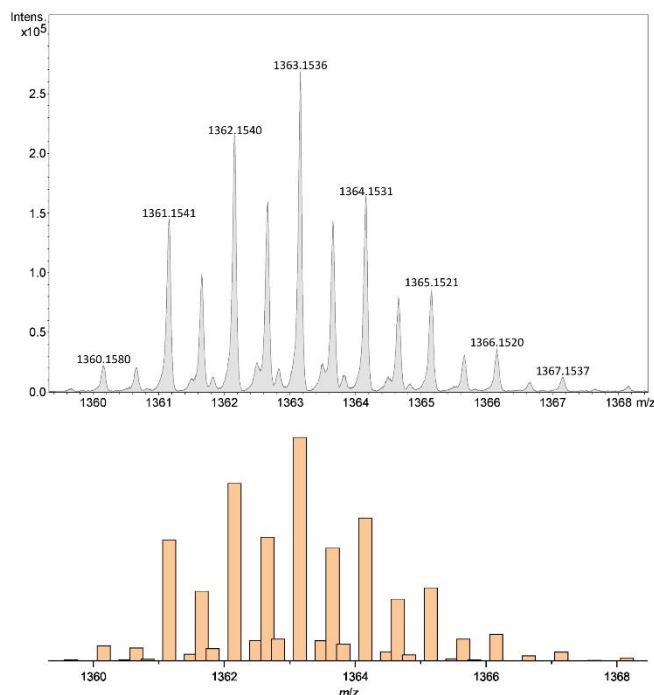


Figure 5 Top: expansion of the principal high mass peak in the electrospray mass spectrum of **1[ClO₄]₄** from MeCN solution. Bottom: simulation of the peak as a 0.3:0.6:0.1 mixture of $[\text{Fe}_2(L^1)_2(\text{ClO}_4)_3]^+$, $[\text{Fe}_4(L^1)_4(\text{ClO}_4)_6]^{2+}$ and $[\text{Fe}_6(L^1)_6(\text{ClO}_4)_9]^{3+}$.

The ^1H NMR spectrum of **3[ClO₄]₂** in CD_3CN is complex, with multiple paramagnetic L^3 environments. The spectrum in $(\text{CD}_3)_2\text{CO}$ is simpler, however, with three main L^3 -containing species being present (Figure S40). Hence, the composition of assembly structures in solutions of **3[ClO₄]₂** may be solvent-dependent. Be that as it may, solutions of **3[ClO₄]₂** are a more complex mixture of assembly structures by NMR, in slow chemical exchange. That should explain the amorphous nature of the materials formed by those complexes in the solid state.

Gas phase DFT calculations were undertaken to investigate the influence of the different conformations exhibited by **1[BF₄]₂** on its spin state (Figure 1); and, to probe the stability of the helicite structures more generally.^[54,55] The calculations employed the B86PW91 functional and def2-SVP basis set, which we have used successfully in comparative studies of the spin states in mononuclear iron(II) complexes of bpp derivatives or related ligands.^[56-59] Closely related GGA functionals have also performed well in surveys of functionals for SCO systems.^[60]

Conformations (a)-(c) of $[\text{Fe}_2(\mu-L^1)_2]^{4+}$ (Figure 1), and $[\text{Fe}_2(\mu-L^2)_2]^{4+}$, were minimized in their low-spin (LS, $S = 0$), mixed-spin (MS, $S = 2$) and fully high-spin (HS, $S = 4$) states. The spin states of mononuclear $[\text{FeL}^1]^{2+}$ were also minimized, for comparison. These calculations highlighted unexpected anomalies. Firstly, $[\text{Fe}_2(\mu-L^1)_2]^{4+}$ was computed to be at least +100 kcal mol⁻¹ higher energy than $[\text{FeL}^1]^{2+}$ (per mole of dimer), implying the helicite complex should not exist (Table S8). Secondly, the energy difference between the high-spin and low-spin states $[\Delta E(\text{HS}-\text{LS})]$, Table 3) of $[\text{Fe}_2(\mu-L^1)_2]^{4+}$ is ca 3x larger than for 2 equiv of $[\text{FeL}^1]^{2+}$. That suggests the low-spin state of the helicites is over-stabilized by the calculation. Lastly, the Fe \cdots Fe distances in minimized

Table 3. Computed energies of the high-spin (HS, $S = 4$), mixed-spin (MS, $S = 2$) and low-spin (LS, $S = 0$) states of the iron complexes in this work. Energies of the corresponding chromium complex minimizations are listed in Table S9.

	$E(\text{HS})$ [Ha]	$E(\text{MS})$ [Ha]	$E(\text{LS})$ [Ha]	$\Delta E\{\text{HS-LS}\}$ [kcal mol ⁻¹]	$\Delta E_{\text{rel}}\{\text{HS-LS}\}$ [kcal mol ⁻¹] ^[a]	$\Delta E\{\text{HS-LS, MS}\}$ [kcal mol ⁻¹] ^[b]
$[\text{FeL}^1]^{2+}$	-2815.484288	-	-2815.490595	+4.0	-	-
$[\text{Fe}_2(\mu\text{-L}^1)_2]^{4+}$, conformation (a)	-5630.785068	-5630.802870	-5630.820271	+22.1	0	+0.1
$[\text{Fe}_2(\mu\text{-L}^1)_2]^{4+}$, conformation (b)	-5630.786168	-5630.802732	-5630.819907	+21.2	-0.9	-0.2
$[\text{Fe}_2(\mu\text{-L}^1)_2]^{4+}$, conformation (c)	-5630.788009	-5630.802622	-5630.818614	+19.2	-2.9	-0.4
$[\text{Fe}_2(\mu\text{-L}^2)_2]^{4+}$	-5810.391891	-5810.402230	-5810.409082	+10.8	-11.3	+1.1
$[\text{Fe}_2(\mu\text{-L}^3)_2]^{4+}$	-5935.545352	-5935.560026	-5935.572551	+17.1	-5.0	+0.7

[a] A positive $\Delta E_{\text{rel}}\{\text{HS-LS}\}$ means the low-spin state is more stable than for conformation (a) of $[\text{Fe}_2(\mu\text{-L}^1)_2]^{4+}$ ($M = \text{Fe}^{2+}$ or Cr^0), and *vice versa*. [b] A positive $\Delta E\{\text{HS-LS, MS}\}$ means the mixed-spin state is more stable than an equimolar mixture of high-spin and low-spin molecules, and *vice versa*.

$[\text{Fe}_2(\mu\text{-L}^1)_2]^{4+}$ are consistently 0.4-1.2 Å longer than the crystallographic values; for $[\text{Fe}_2(\mu\text{-L}^2)_2]^{4+}$, the difference is 2.3 Å (Tables S10 and S11). All these observations can be explained, if the calculations are influenced by intramolecular electrostatic repulsion between the Fe^{2+} ions in the dinuclear complexes.^[14] Such electrostatic effects could be significant in the gas phase but should be reduced in condensed phases, by ion pairing and dipolar interactions to a solvent shell or crystal lattice.

Since a solvent correction could not be included in our calculations,^[54] this anomaly was addressed by gas-phase minimizations of the isoelectronic charge-neutral molecules $[\text{Cr}_2(\mu\text{-L})_2]^0$ and $[\text{CrL}]^0$ (Tables S8-S9). The computed structures of the low-spin chromium complexes agree with expectation. However mixed-spin or high-spin chromium(0) minimizations yielded results that are more consistent with chromium(II) centers coordinated to $[\text{L}]^-$ ligand radicals. That was evidenced by their chromium coordination geometries, which are strongly Jahn-Teller-elongated (Tables S12-S13); and, by their α and β HOMO orbitals, which are ligand-centered in these chromium minimizations but metal-centered in their iron(II) counterparts (Figures S46-S47).^[55] Within that generalization, differences between the computed high-spin chromium centers suggest additional subtleties, which are beyond the scope of this study.^[61] Because of these ambiguities, only the minimizations of the low-spin chromium complexes are analyzed in detail

Despite these complications, some conclusions can be drawn from the analysis. In contrast to its iron analogue, low-spin $[\text{Cr}_2(\mu\text{-L}^1)_2]^0$ is computed to be -27 kcal mol⁻¹ lower energy than mononuclear $[\text{CrL}^1]^0$, which now agrees with experiment. The $\Delta E\{\text{HS-LS}\}$ energies of $[\text{CrL}^1]^0$ and $[\text{Cr}_2(\mu\text{-L}^1)_2]^0$ are also more consistent with each other, than for the iron complexes (Table S8). Lastly, the metal...metal distances in each low-spin $[\text{M}_2(\mu\text{-L})_2]^{2z+}$ complex are 0.4-0.6 Å shorter when $M = \text{Cr}(0)$ than when $M = \text{Fe}(II)$ (Tables S10-S13). All these observations imply electrostatic repulsion between the iron atoms is indeed an important factor in our gas phase minimizations of $[\text{Fe}_2(\mu\text{-L})_2]^{4+}$.

The three conformations of the iron complex, in a given spin state, are within 2 kcal mol⁻¹ of each other by this protocol. The

difference is smaller for low-spin $[\text{Cr}_2(\mu\text{-L}^1)_2]^0$, where conformations (a)-(c) lie within 0.7 kcal mol⁻¹ (Table S9). Hence, all these conformations should be thermally accessible at room temperature, as observed. More detailed discussion of the minimized structures is not justified however, because of the ambiguities noted above.

The absolute spin state energies from a protocol like this are inaccurate, so the $\Delta E_{\text{rel}}\{\text{HS-LS}\}$ energies in Tables 3 and S9 are scaled relative to conformation (a) of the relevant $[\text{M}_2(\mu\text{-L}^1)_2]^{2z+}$ molecule. A molecule with a positive $\Delta E_{\text{rel}}\{\text{HS-LS}\}$ has a more stable low-spin state than conformation (a), and so should exhibit a higher $T_{1/2}$ value. Similarly, a negative $\Delta E_{\text{rel}}\{\text{HS-LS}\}$ implies $T_{1/2}$ should be lower than conformation (a). By this measure, $T_{1/2}$ for the conformations of $[\text{Fe}_2(\mu\text{-L}^1)_2]^{4+}$ should follow the trend of (a) > (b) > (c). That is broadly consistent with the crystallographic and magnetic properties of the **1** $[\text{BF}_4]_2$ solvates (Table 1, Figure 3).

The mixed-spin forms of $[\text{Fe}_2(\mu\text{-L}^1)_2]^{4+}$ have almost identical energy to an equimolar mixture of high-spin and low-spin molecules, to within 0.5 kcal mol⁻¹ ($\Delta E\{\text{HS-LS, MS}\}$, Table 3). Thus, the mixed-spin form of **1** $[\text{BF}_4]_2$ is not intrinsically electronically favored. The stepwise SCO in **1** $[\text{BF}_4]_4 \cdot n\text{Me}_2\text{CO}$, and the incomplete SCO in **1** $[\text{BF}_4]_4 \cdot 2\text{MeCN} \cdot \text{Et}_2\text{O}$, should therefore be a consequence of solid state packing effects.

$[\text{Fe}_2(\mu\text{-L}^2)_2]^{4+}$ is computed with a large, negative $\Delta E_{\text{rel}}\{\text{HS-LS}\}$ value, showing it is strongly high-spin as observed. However, all the spin states of $[\text{M}_2(\mu\text{-L}^2)_2]^{2z+}$ ($M^{z+} = \text{Fe}^{2+}$ or Cr^0) minimized to a more symmetric L^2 ligand conformation than found crystallographically for **2** $[\text{ClO}_4]_2$. This places the metal atoms further apart, and with a less distorted coordination geometry than found experimentally.^[55] Since the structure should reflect both the conformational preferences of L^2 and ligand field effects on the metal geometry, our DFT protocol may over-estimate the ligand field contribution to the structure of this molecule. Consistent with that, molecular mechanics minimizations of $[\text{M}_2(\mu\text{-L}^2)_2]^{2z+}$, which exclude ligand field considerations, reproduced the experimental conformation of **2** $[\text{ClO}_4]_2$ more accurately (Figure 6).

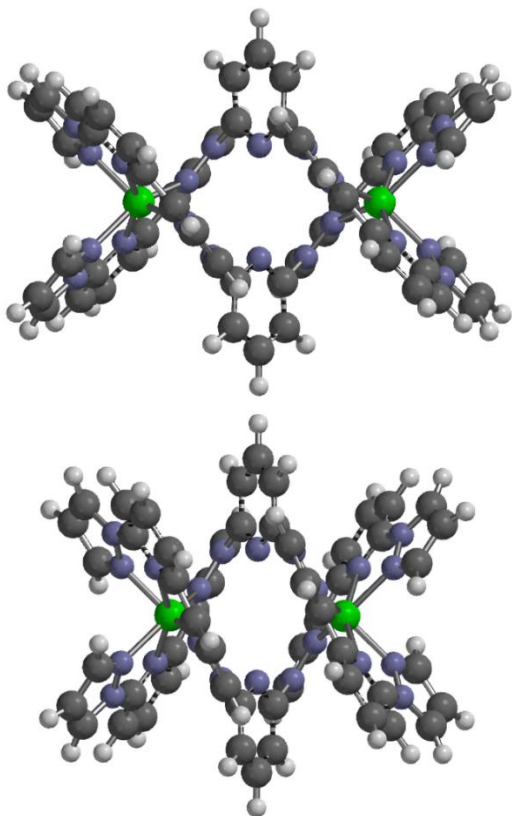


Figure 6. Computed structures of $[\text{Fe}_2(\mu\text{-}L^2)_2]^{4+}$. Top: DFT energy minimization of the high-spin ($S = 4$) iron complex ($\text{Fe}\cdots\text{Fe} = 7.418 \text{ \AA}$). Bottom: molecular mechanics geometry minimization ($\text{M}\cdots\text{M} = 5.356 \text{ \AA}$). The molecular mechanics calculation is closer to the experimental structure (Table 2, Figure 4). Color code: C, gray; H, white; N, blue; Fe or M, green.

Minimizations of the $[\text{M}_2(\mu\text{-}L^3)_2]^{2z+}$ helicate were also investigated.^[55] These also revealed conformational flexibility in the xylyl linker group, placing the metal atoms in the low-spin iron complex 0.9 \AA further apart than in the chromium compound (Figure S48). MM2 minimizations reproduced the chromium complex conformation, so the extended conformation of $[\text{Fe}_2(\mu\text{-}L^3)_2]^{4+}$ could again reflect electrostatic repulsion between its Fe^{2+} ions. The high-spin state of $[\text{Fe}_2(\mu\text{-}L^3)_2]^{4+}$ is significantly stabilized compared to $[\text{Fe}_2(\mu\text{-}L^1)_2]^{4+}$ (Table 3), which is consistent with the high-spin nature of $3\mathbf{X}_2$ at room temperature. However, since no crystallographic data are available for the Fe/L^3 complex, the relevance of these results to its experimental properties is unclear.

Conclusion

Four new ditopic ligands have been synthesized, by connecting two 1,3-bpp metal-binding moieties with different spacers *via* their distal N–H groups. Two of these, L^1 and L^2 , cleanly afford $[2+2]$ helicate complexes when complexed to iron(II). Three helical conformations of $[\text{Fe}_2(\mu\text{-}L^1)_2]^{4+}$ were observed in different solvate crystals of $1[\text{BF}_4]_4$ (Figure 1), which exhibit a range of spin state properties. These include a clear, unusual stepwise SCO of the two iron centers in $1[\text{BF}_4]_4 \cdot n\text{Me}_2\text{CO}$, *via* a mixed-spin intermediate which was detected crystallographically (Figure 3).^[62] The DFT calculations imply conformations (a)–(c) of $[\text{Fe}_2(\mu\text{-}L^1)_2]^{4+}$ should all exist in solution, while NMR showed they are in rapid chemical exchange at room temperature. Hence, the

observation of different helicate conformations in crystals of $1[\text{BF}_4]_4$ should simply reflect the crystal packing in each solvate.

In contrast, salts of $[\text{Fe}_2(\mu\text{-}L^2)_2]^{4+}$ remain high-spin at all temperatures. That is explained by the molecular conformation shown by $2[\text{ClO}_4]_4$, which leads to the most distorted six-coordinate geometries yet observed in the extended family of $[\text{Fe}(\text{bpp})_2]^{2+}$ SCO materials (Figures 2 and 4). Analytically pure iron(II) complexes of L^3 were also obtained, which are however completely amorphous in the solid state. Hence, the molecular structures of $3[\text{BF}_4]_2$ and $3[\text{ClO}_4]_2$ are uncertain.

Solutions of $1[\text{ClO}_4]_4$, $2[\text{ClO}_4]_4$ and $3[\text{ClO}_4]_2$ contain both $[\text{Fe}_2(\mu\text{-}L)_2]^{4+}$ and $[\text{Fe}_4(\mu\text{-}L)_4]^{8+}$ ($L = L^1\text{-}L^3$) by mass spectrometry, with higher nuclearity species also being present in some cases (Figures 5 and S35–S37). Hence, the helicate complexes exist in equilibrium with other assembly structures in solution. That being the case, ^1H NMR implies those assemblies interconvert in solution more rapidly when $L = L^1$ than for the more rigid $L = L^2$ or L^3 . Hence, the identity of the spacer group strongly influences the composition and dynamics of the supramolecular assemblies formed by $L^1\text{-}L^3$.

Gas phase DFT calculations confirm conformations (a)–(c) of $[\text{Fe}_2(\mu\text{-}L^1)_2]^{4+}$ have almost identical energies, but should show detectably different spin state properties. These appear consistent with experiment, in that the computed spin state energies mirror the observed trend in solid state SCO temperatures, of conformation (a) > (b) > (c) (Figure 3, Table 3). The calculations also reproduce the high-spin nature of $[\text{Fe}_2(\mu\text{-}L^2)_2]^{4+}$. However in other respects the calculations present anomalies, which are consistent with the influence of intramolecular electrostatic repulsion between the positively charged iron ions. Such effects would be compensated in condensed phases, by ion pairing and weaker intermolecular dipolar interactions with the surrounding medium. That could lead to significant discrepancies between the results of our single point calculations and experiment, as observed. Further calculations of isoelectronic $[\text{Cr}_2(\mu\text{-}L^1)_2]^0$ and $[\text{Cr}_2(\mu\text{-}L^2)_2]^0$ support that view, but were themselves only partly successful because the high-spin chromium(0) centers undergo valence tautomeric oxidation to chromium(II) *in silico*.

Other gas phase DFT studies on dinuclear^[63] or higher nuclearity^[14,53,64] SCO complexes have investigated more conformationally rigid molecules, many of which are electroneutral. The influence of intramolecular electrostatic effects on the calculations should be less apparent in those cases. However, a recent gas phase DFT study of Fe_4 grid complexes noted that the high-spin states of more highly charged molecules in that study were over-stabilized computationally, compared to their uncharged analogues.^[14] Electrostatic interactions between the iron atoms in those molecules were proposed to contribute to that discrepancy. In contrast, the low-spin state of the dinuclear complexes appears to be over-stabilized in this work (Tables 3 and S9), although we base that observation on different criteria from those in ref. [14]. In other respects, our results are consistent with the conclusions from that earlier study.^[65]

Experimental Section

Instrumentation

Solid state magnetic susceptibility measurements were performed with freshly isolated, unground polycrystalline samples, using a Quantum Design MPMS-3 SQUID/VSM magnetometer in an applied field of 5000 G. Samples were protected against solvent loss by saturating the tightly sealed MPMS-3 powder capsules with diethyl ether vapor, Unless otherwise specified, the measurements employed a temperature ramp of 5 Kmin⁻¹. Diamagnetic corrections for the samples were estimated from Pascal's constants;^[66] a previously measured diamagnetic correction for the sample holder was also applied to the data.

Elemental microanalyses were performed by the microanalytical services at London Metropolitan University School of Human Sciences. Electrospray mass spectra were recorded on a Bruker MicroTOF-q instrument from chloroform (organic ligands) or acetonitrile (metal complexes) solution. The peak simulations in Figures 5, S36 and S37 were plotted with *ORIGIN*,^[67] starting from simulations of the individual component species produced by *Bruker Compass*.^[68] Diamagnetic NMR spectra employed a Bruker AV3HD spectrometer operating at 400.1 (¹H) or 100.6 MHz (¹³C), while paramagnetic ¹H NMR spectra were obtained with a Bruker AV3 spectrometer operating at 300.1 MHz. X-ray powder diffraction measurements were obtained at room temperature from a Bruker D2 Phaser diffractometer, using Cu-K_α radiation ($\lambda = 1.5419 \text{ \AA}$).

All calculations were performed using *SPARTAN'18*.^[69] DFT calculations employed the B86PW91 functional and def2-SVP basis set. Low-spin systems were treated as spin restricted and high-spin systems as spin unrestricted. The calculations were performed in the gas phase, since a solvent gradient for iron is not implemented in *SPARTAN'18*. Crystallographic atomic coordinates for the different conformations of **12⁺**, and for **22⁺**, were used as a starting point for those geometry minimizations. Otherwise, initial models were constructed *de novo* in the program, then subjected to a preliminary molecular mechanics minimization before the full DFT energy minimization was undertaken.

Molecular mechanics (MM) structures were calculated in *SPARTAN'18*^[69] for the chromium complexes [Cr₂(μ -L¹)₂]⁰ and [Cr₂(μ -L²)₂]⁰, since the atomic radius of chromium in the MM minimization protocol resembles that of high-spin iron(II) [Cr-N *ca* 2.2 Å]. This was preferred over analogous MM calculations using the Fe₂ helicate molecules, which yielded unrealistically short Fe-N distances [Fe-N *ca* 1.8 Å].

Materials and Methods.

Synthetic protocols and characterization data for L¹-L⁴ and the other new compounds in Scheme 1, are given in the Supporting Information.

CAUTION We experienced no problems when using the perchlorate salts in this study. However, metal-organic perchlorates are potentially explosive and should be handled with care in small quantities.

Synthesis of [Fe₂(μ -L¹)₂][BF₄]₄ (1[BF₄]₄). A mixture of L¹ (0.20 g, 0.42 mmol) and Fe[BF₄]₂·6H₂O (0.14 g, 0.42 mmol) in nitromethane (25 cm³) was stirred at room temperature for 1 hr. A small quantity of brown precipitate was removed by filtration, and the dark yellow filtrate was concentrated to half its original volume. Slow diffusion of diethyl ether vapor into the filtered solution afforded an orange polycrystalline solid, which turned brown when dried *in vacuo*. Yield 0.19 g, 64 %. Elemental analysis calcd (%) for C₅₂H₄₈B₄F₁₆Fe₂N₂₀·2CH₃NO₂·2H₂O C 41.3, H 3.72, N 19.6; found C 41.1, H 3.29, N 19.3.

Synthesis of [Fe₂(μ -L¹)₂][ClO₄]₄ (1[ClO₄]₄). Method as for **1[BF₄]₂**, using Fe[ClO₄]₂·6H₂O (0.15 g, 0.42 mmol). The product was an orange polycrystalline solid, which turned brown upon drying. Yield 0.15 g, 49 %. ¹H NMR (CD₃CN): $\delta = -13.8$ (4H), -10.6 (4H), -7.0 (4H), 5.6 (4H), 12.4 (4H), 23.8 (4H), 41.8 (4H), 44.2 (4H), 56.7 (4H), 60.3 (4H), 69.8 (4H), 71.0 (4H); HRMS (ESI): *m/z* calcd for C₂₆H₂₄N₁₀+Na⁺: 499.2083 [L¹+Na]⁺; found: 499.2023; calcd for C₂₆H₂₄ClFeN₁₀O₄⁺: 631.1020 [Fe(L¹)ClO₄]⁺; found: 631.0929; calcd for {C₅₂H₄₈Cl₃Fe₂N₂₀O₁₂}_z^{z+}: 1363.1525 [Fe₂(L¹)₂(ClO₄)_{3z}]^{z+}; found: 1363.1526. The peak at *m/z* 1363.1526 is an overlay of monocation (*z* = 1), dication (*z* = 2) and trication (*z* = 3) molecular ions; elemental analysis calcd (%) for C₅₂H₄₈Cl₄Fe₂N₂₀O₁₆·CH₃NO₂·H₂O C 41.3, H 3.47, N 19.1; found C 41.0, H 3.15, N 18.9.

Synthesis of [Fe₂(μ -L²)₂][BF₄]₄ (2[BF₄]₄). A mixture of crude L² (0.20 g, 0.40 mmol) and Fe[BF₄]₂·6H₂O (0.14 g, 0.40 mmol) in nitromethane (25 cm³) was stirred with mild heating, until all the solid had dissolved. The bright yellow solution was filtered and concentrated to *ca* 5 cm³ volume. Slow diffusion of diethyl ether vapor into the filtered solution afforded a yellow crystalline solid, which decomposes to a yellow powder on exposure to air. Yield 0.21 g, 72 %. Elemental analysis calcd (%) for C₅₄H₃₈B₄F₁₆Fe₂N₂₂·H₂O 44.1, H 2.74, N 20.9; found C, 44.2, H, 2.43, N, 20.6.

Synthesis of [Fe₂(μ -L²)₂][ClO₄]₄ (2[ClO₄]₄). Method as for **2[BF₄]₂**, using Fe[ClO₄]₂·6H₂O (0.15 g, 0.40 mmol). The product was a yellow polycrystalline solid. Yield 0.22 g, 73 %. ¹H NMR (CD₃CN): $\delta = -2.3$ (4H), 0.9 (2H), 18.6 (4H), 36.1 (4H), 55.7 (4H), 56.7 (4H), 58.9 (4H), 68.8 (8H), 76.4 (4H). At least one other paramagnetic L²-containing species is also present in the spectrum, with 10-15 % of the integral compared to the main component; HRMS (ESI): *m/z* calcd for C₅₄H₃₈FeN₂₂²⁺: 525.1495 [Fe(L²)₂]²⁺; found: 525.1571; calcd for {C₂₇H₁₉ClFeN₁₁O₄}_z^{z+}: 652.0659 [Fe_z(L²)_z(ClO₄)_z]^{z+}; found: 652.0635; calcd for C₂₇H₁₉Cl₃Fe₂N₁₁O₁₂⁺: 905.8979 [Fe₂(L²)(ClO₄)₃]⁺; found: 905.8891; calcd for C₅₄H₃₈ClFeN₂₂O₄⁺: 1149.2484 [Fe(L²)₂ClO₄]⁺; found: 1149.2385; calcd for {C₅₄H₃₈Cl₃Fe₂N₂₂O₁₂}_z^{z+}: 1405.0775 [Fe₂(L²)₂(ClO₄)_{3z}]^{z+}; found: 1405.0681. The peaks at *m/z* 652.0635 and 1405.0681 are an overlays of monocation (*z* = 1) and dication (*z* = 2) molecular ions; elemental analysis calcd (%) for C₅₄H₃₈Cl₄Fe₂N₂₂O₁₆ C 43.1, H 2.55, N 20.5; found C 43.2, H 2.50, N 20.3.

Synthesis of {[Fe(L³)](BF₄)₂}_x·xCH₃NO₂ (3[BF₄]₂·CH₃NO₂). A mixture of L³ (0.15 g, 0.29 mmol) and Fe[BF₄]₂·6H₂O (0.10 g, 0.29 mmol) in nitromethane (20 cm³) was stirred at room temperature until all the solid had dissolved. A small quantity of brown

precipitate was removed by filtration, and the yellow filtrate was concentrated to half its original volume. Slow diffusion of diethyl ether vapor into the filtered solution afforded a glassy orange solid. Yield 0.11 g, 50 %. Elemental analysis calcd (%) for $C_{30}H_{24}B_2F_8FeN_{10} \cdot CH_3NO_2 \cdot C$ 45.7, H 3.34, N 18.9; found C 45.2, H 3.21, N 19.1.

Synthesis of $\{[Fe(L^3)](ClO_4)_2\}_x \cdot 1.5xH_2O$ ($3[ClO_4]_2 \cdot 1.5H_2O$). Method as for $3[BF_4]_2$, using $Fe[ClO_4]_2 \cdot 6H_2O$ (0.11 g, 0.29 mmol). The product was a glassy orange solid. Yield 0.15 g, 66 %. The 1H NMR spectrum of this product is complex, containing multiple paramagnetic iron/ L^3 environments (Figure S40). HRMS (ESI): m/z calcd for $C_{30}H_{24}ClFeN_{10}O_4^+$: 679.1020 $[Fe(L^3)ClO_4]^+$; found: 679.0993; calcd for $\{C_{60}H_{48}Cl_3Fe_2N_{20}O_{12}\}_z^{z+}$: 1459.1525 $[Fe_2(L^3)_2(ClO_4)_3]^{2+}$; found: 1459.1513; calcd for $C_{150}H_{120}Cl_8Fe_5N_{50}O_{32}^+$: 1848.6690 $[Fe_5(L^3)_5(ClO_4)_8]^{2+}$; found: 1848.6669. The peak at m/z 1459.1513 is an overlay of monocation ($z = 1$) and dication ($z = 2$) molecular ions; elemental analysis calcd (%) for $C_{30}H_{24}Cl_2FeN_{10}O_8 \cdot 1.5H_2O \cdot C$ 44.7, H 3.37, N 17.4; found C 44.7, H 3.36, N 16.9.

Crystal Structure Analyses

Crystals of 1,3-bpp were grown by slow evaporation of an NMR sample of the compound in $CDCl_3$. The solvent-free crystals $2[ClO_4]_4$ were obtained by slow diffusion of diethyl ether vapor into a filtered solution of the complex in acetone. The other solvated crystals were grown similarly, by diethyl ether vapor diffusion in the appropriate solvent. Diffraction data for $1[BF_4]_4 \cdot nMe_2CO$ were recorded at station I19 of the Diamond synchrotron ($\lambda = 0.6889$ Å). All other diffraction data were measured with an Agilent Supernova dual-source diffractometer using monochromated $Cu-K\alpha$ ($\lambda = 1.5418$ Å) radiation. The diffractometer was fitted with an Oxford Cryostream low-temperature device.

Crystallographic experimental details and refinement protocols are given in the Supporting Information. All the structures were solved by direct methods (*SHELXS*^[70]), and developed by full least-squares refinement on F^2 (*SHELXL-2018*^[70]). Crystallographic figures were prepared using *XSEED*,^[71] while calculation of structural indices and preparation of publication materials was performed with *Olex2*.^[72]

Deposition numbers 2169630 (α -1,3-bpp), 2169631 ($1[BF_4]_4 \cdot nMe_2CO$, $T = 250$ K), 2169632 ($1[BF_4]_4 \cdot nMe_2CO$, $T = 100$ K), 2169633 ($1[BF_4]_4 \cdot 2MeCN \cdot Et_2O$), 2169634 ($1[BF_4]_4 \cdot mMeNO_2$), 2169635 ($1[BF_4]_4 \cdot 2MeNO_2$), 2169636 ($2[ClO_4]_4$) and 2169637 ($2[ClO_4]_4 \cdot 3MeNO_2 \cdot 0.75H_2O$) contain the supplementary crystallographic data for this paper. These data are provided free of charge by the joint Cambridge Crystallographic Data Centre and Fachinformationszentrum Karlsruhe Access Structures service.

Acknowledgements

This work was funded by the EPSRC (EP/K012576/1) and the University of Leeds. We acknowledge Diamond Light Source for access to beamline I19 (MT-15059), which contributed to the results presented here. The authors also thank Drs. Izar Capel

Berdiell, Namrah Shahid and Iurii Galadzhun (University of Leeds) for help with some measurements, and Dr Sergi Vela (University of Barcelona) for useful discussions.

Conflict of Interest

The authors declare no conflict of interest.

Data Availability Statement

Data supporting this study are openly available from the University of Leeds library at <http://doi.org/10.5518/1205>.

Keywords: spin-crossover • iron • N-ligands • self-assembly • helicate complexes

- [1] *Spin Crossover in Transition Metal Compounds I – III, Topics in Current Chemistry, Vol. 233–235* (Eds.: P. Gütllich, H. A. Goodwin), Springer, New York, **2004**.
- [2] *Spin-Crossover Materials—Properties and Applications* (Ed. M. A. Halcrow), Wiley, Chichester, **2013**, p. 568.
- [3] J. Zarembowitch, F. Varret, A. Hauser, J. A. Real, K. Boukheddaden, *C. R. Chimie* **2018**, *21*, 1056–1059.
- [4] Recent reviews of general SCO chemistry: a) O. Sato, *Nature Chem.* **2016**, *8*, 644–656; b) K. Senthil Kumar, M. Ruben, *Coord. Chem. Rev.* **2017**, *346*, 176–205. c) Z.-S. Yao, Z. Tang, J. Tao, *Chem. Commun.* **2020**, *56*, 2071–2086. d) P. Guionneau, M. Marchivie, G. Chastanet, *Chem. - Eur. J.* **2021**, *27*, 1483–1486.
- [5] a) O. Kahn, J. Krober, C. Jay, *Adv. Mater.* **1992**, *4*, 718–728; b) A. B. Gaspar, V. Ksenofontov, M. Seredyuk, P. Gütllich, *Coord. Chem. Rev.* **2005**, *249*, 2661–2676; c) M. Clemente-León, E. Coronado, C. Martí-Gastaldo, F. M. Romero, *Chem. Soc. Rev.* **2011**, *40*, 473–497; d) A. Enriquez-Cabrera, A. Rapakousiou, M. Piedrahita Bello, G. Molnár, L. Salmon, A. Bousseksou, *Coord. Chem. Rev.* **2020**, *419*, 213396; e) M. Wang, Z.-Y. Li, R. Ishikawa, M. Yamashita, *Coord. Chem. Rev.* **2021**, *435*, 213819.
- [6] Selected recent examples: a) M. D. Manrique-Juarez, F. Mathieu, A. Laborde, S. Rat, V. Shalabaeva, P. Demont, O. Thomas, L. Salmon, T. Leïchlé, L. Nicu, G. Molnár, A. Bousseksou, *Adv. Funct. Mater.* **2018**, *28*, 1801970; b) S. P. Vallone, A. N. Tantillo, A. M. dos Santos, J. Molaison, R. Kulmaczewski, A. Chapoy, P. Ahmadi, M. A. Halcrow, K. G. Sandeman, *Adv. Mater.* **2019**, *31*, 1807334; c) K. Ridier, Y. Zhang, M. Piedrahita-Bello, C. M. Quintero, L. Salmon, G. Molnár, C. Bergaud, A. Bousseksou, *Adv. Mater.* **2020**, *32*, 2000987; d) M. Piedrahita-Bello, J. E. Angulo-Cervera, R. Courson, G. Molnár, L. Malaquin, C. Thibault, B. Tondou, L. Salmon, A. Bousseksou, *J. Mater. Chem. C* **2020**, *8*, 6001–6005; e) Z. G. Lada, K. S. Andrikopoulos, G. N. Mathioudakis, Z. Piperigkou, N. Karamanos, S. P. Perlepes, G. A. Voyiatzis, *Magnetochemistry* **2022**, *8*, 16.
- [7] a) G. Molnár, S. Rat, L. Salmon, W. Nicolazzi, A. Bousseksou, *Adv. Mater.* **2018**, *30*, 1703862; b) E. Coronado, *Nature Rev. Mater.* **2020**, *5*, 87–104; c) K. Senthil Kumar, M. Ruben, *Angew. Chem. Int. Ed.* **2021**, *60*, 7502–7521; *Angew. Chem.* **2021**, *133*, 7578–7598; d) L. Kippen, M. Bernien, F. Tuczek, W. Kuch, *Adv. Mater.* **2021**, *33*, 2008141 and **2021**, *33*, 2170354 [correction].
- [8] a) R. W. Hogue, S. Singh, S. Brooker, *Chem. Soc. Rev.* **2018**, *47*, 7303–7338; b) A. J. McConnell, *Supramol. Chem.* **2018**, *30*, 858–868.
- [9] W. Huang, X. Ma, O. Sato, D. Wu, *Chem. Soc. Rev.* **2021**, *50*, 6832–6870.
- [10] A. J. McConnell, C. M. Aitchison, A. B. Grommet, J. R. Nitschke, *J. Am. Chem. Soc.* **2017**, *139*, 6294–6297.
- [11] W.-K. Han, H.-X. Zhang, Y. Wang, W. Liu, X. Yan, T. Li, Z.-G. Gu, *Chem. Commun.* **2018**, *54*, 12646–12649.

- [12] a) M. Darawsheh, L. A. Barrios, O. Roubeau, S. J. Teat, G. Aromí, *Chem. – Eur. J.* **2016**, *22*, 8635–8645; b) M. Darawsheh, L. A. Barrios, O. Roubeau, S. J. Teat, G. Aromí, *Angew. Chem. Int. Ed.* **2018**, *57*, 13509–13513; *Angew. Chem.* **2018**, *130*, 13697–13701; c) D. Yu. Aleshin, R. Diego, L. A. Barrios, Y. V. Nelyubina, G. Aromí, V. V. Novikov, *Angew. Chem. Int. Ed.* **2022**, *61*, e202110310; *Angew. Chem.* **2022**, *134*, e202110310; d) L. A. Barrios, R. Diego, M. Darawsheh, J. I. Martínez, O. Roubeau, G. Aromí, *Chem. Commun.* **2022**, *58*, 5375–5378.
- [13] a) M. Estrader, J. S. Uber, L. A. Barrios, J. Garcia, P. Lloyd-Williams, O. Roubeau, S. J. Teat, G. Aromí, *Angew. Chem. Int. Ed.* **2017**, *56*, 15622–15627; *Angew. Chem.* **2017**, *129*, 15828–15833; b) Z.-Y. Li, J.-W. Dai, M. Damjanović, T. Shiga, J.-H. Wang, J. Zhao, H. Oshio, M. Yamashita, X.-H. Bu, *Angew. Chem. Int. Ed.* **2019**, *58*, 4339–4344; *Angew. Chem.* **2019**, *131*, 4383–4388.
- [14] S. Dhers, A. Mondal, D. Aguilà, J. Ramírez, S. Vela, P. Dechambenoit, M. Rouzières, J. R. Nitschke, R. Clérac, J.-M. Lehn, *J. Am. Chem. Soc.* **2018**, *140*, 8218–8227.
- [15] Other recent examples of SCO molecular squares and grids: a) T. Shiga, Y. Sato, M. Tachibana, H. Sato, T. Matsumoto, H. Sagayama, R. Kumai, Y. Murakami, G. N. Newton, H. Oshio, *Inorg. Chem.* **2018**, *57*, 14013–14017; b) C. Zheng, S. Jia, Y. Dong, J. Xu, H. Sui, F. Wang, D. Li, *Inorg. Chem.* **2019**, *58*, 14316–14324; c) K. Kaushik, S. Ghosh, S. Kamilya, M. Rouzières, S. Mehta, A. Mondal, *Inorg. Chem.* **2021**, *60*, 7545–7552; d) Z. Guo, M. You, Y.-F. Deng, Q. Liu, Y.-S. Meng, Z. Pikramenou, Y.-Z. Zhang, *Dalton Trans.* **2021**, *50*, 14303–14308; e) M. You, G. T. Nguyen, D. Shao, T. Wang, X.-Y. Chang, L. Ungur, Y.-Z. Zhang, *Dalton Trans.* **2022**, *51*, 5596–5602.
- [16] a) H. S. Scott, R. W. Staniland, P. E. Kruger, *Coord. Chem. Rev.* **2018**, *362*, 24–43; b) K. Senthil Kumar, Y. Bayeh, T. Gebretsadik, F. Elemo, M. Gebrezgiabher, M. Thomas, M. Ruben, *Dalton Trans.* **2019**, *48*, 15321–15337.
- [17] a) T. F. Miller, L. R. Holloway, P. P. Nye, Y. Lyon, G. J. O. Beran, W. H. Harman, R. R. Julian, R. J. Hooley, *Inorg. Chem.* **2018**, *57*, 13386–13396; b) S. Singh, R. W. Hogue, H. L. C. Feltham, S. Brooker, *Dalton Trans.* **2019**, *48*, 15435–15444.
- [18] Other recent examples of tetrahedral SCO cage complexes: a) L. Li, A. R. Craze, O. Mustonen, H. Zenno, J. J. Whittaker, S. Hayami, L. F. Lindoy, C. E. Marjo, J. K. Clegg, J. R. Aldrich-Wright, F. Li, *Dalton Trans.* **2019**, *48*, 9935–9938; b) T. Tanaka, Y. Sunatsuki, T. Suzuki, *Inorg. Chim. Acta* **2020**, *502*, 119373; c) W. Li, L. Sun, C. Liu, A. Rotaru, K. Robeyns, M. L. Singleton, Y. Garcia, *J. Mater. Chem. C* **2022**, *10*, 9216–9221; d) W. Li, C. Liu, J. Kfoury, J. Oláh, K. Robeyns, M. L. Singleton, S. Demeshko, F. Meyer, Y. Garcia, *Chem. Commun.* **2022**, *58*, 11653–11656.
- [19] a) N. Struch, C. Bannwarth, T. K. Ronson, Y. Lorenz, B. Mienert, N. Wagner, M. Engeser, E. Bill, R. Puttreddy, K. Rissanen, J. Beck, S. Grimme, J. R. Nitschke, A. Lützen, *Angew. Chem. Int. Ed.* **2017**, *56*, 4930–4935; *Angew. Chem.* **2017**, *129*, 5012–5017; b) M. Hardy, J. Tessarolo, J. J. Holstein, N. Struch, N. Wagner, R. Weisbarth, M. Engeser, J. Beck, S. Horiuchi, G. H. Clever, A. Lützen, *Angew. Chem. Int. Ed.* **2021**, *60*, 22562–22569; *Angew. Chem.* **2021**, *133*, 22736–22743.
- [20] a) I. Capel Berdiell, T. Hochdörffer, C. Desplanches, R. Kulmaczewski, N. Shahid, J. A. Wolny, S. L. Warriner, O. Cespedes, V. Schünemann, G. Chastanet, M. A. Halcrow, *J. Am. Chem. Soc.* **2019**, *141*, 18759–18770; b) H.-S. Lu, W.-K. Han, X. Yan, Y.-X. Xu, H.-X. Zhang, T. Li, Y. Gong, Q.-T. Hua, Z.-G. Gu, *Dalton Trans.* **2020**, *49*, 4220–4224; c) J. Glatz, L.-M. Chamoreau, A. Flambard, J.-F. Meunier, A. Bousseksou, R. Lescouëzec, *Chem. Commun.* **2020**, *56*, 10950–10953.
- [21] a) M. B. Duriska, S. M. Neville, B. Moubaraki, J. D. Cashion, G. J. Halder, K. W. Chapman, C. Balde, J.-F. Létard, K. S. Murray, C. J. Kepert, S. R. Batten, *Angew. Chem. Int. Ed.* **2009**, *48*, 2549–2552; *Angew. Chem.* **2009**, *121*, 2587–2590; b) M. B. Duriska, S. M. Neville, B. Moubaraki, K. S. Murray, C. Balde, J.-F. Létard, C. J. Kepert, S. R. Batten, *ChemPlusChem* **2012**, *77*, 616–623.
- [22] a) S. Chorazy, R. Podgajny, K. Nakabayashi, J. Stanek, M. Rams, B. Sieklucka, S. Ohkoshi, *Angew. Chem. Int. Ed.* **2015**, *54*, 5093–5097; *Angew. Chem.* **2015**, *127*, 5182–5186; b) S. Chorazy, J. J. Stanek, J. Kobylarczyk, S. Ohkoshi, B. Sieklucka, R. Podgajny, *Dalton Trans.* **2017**, *46*, 8027–8036.
- [23] M. Arczyński, M. Rams, J. Stanek, M. Fitta, B. Sieklucka, K. R. Dunbar, D. Pinkowicz, *Inorg. Chem.* **2017**, *56*, 4021–4027.
- [24] a) M. Shatruk, A. Dragulescu-Andrasi, K. E. Chambers, S. A. Stoian, E. L. Bominaar, C. Achim, K. R. Dunbar, *J. Am. Chem. Soc.* **2007**, *129*, 6104–6116; b) K. E. Funck, A. V. Prosvirin, C. Mathonière, R. Clérac, K. R. Dunbar, *Inorg. Chem.* **2011**, *50*, 2782–2789.
- [25] Z. Yan, W. Liu, Y.-Y. Peng, Y.-C. Chen, Q.-W. Li, Z.-P. Ni, M.-L. Tong, *Inorg. Chem.* **2016**, *55*, 4891–4896.
- [26] W. Wen, Y.-S. Meng, C.-Q. Jiao, Q. Liu, H.-L. Zhu, Y.-M. Li, H. Oshio, T. Liu, *Angew. Chem. Int. Ed.* **2020**, *59*, 16393–16397; *Angew. Chem.* **2020**, *132*, 16535–16539.
- [27] T. Shiga, M. Tachibana, H. Sagayama, R. Kumai, G. N. Newton, H. Oshio, M. Nihei, *Chem. Commun.* **2021**, *57*, 10162–10165.
- [28] a) C. Piguat, E. Rivara-Minten, G. Bernardinelli, J.-C. G. Bünzli, G. Hopfgartner, *J. Chem. Soc. Dalton Trans.* **1997**, 421–433; b) C. Edder, C. Piguat, G. Bernardinelli, J. Mareda, C. G. Bochet, J.-C. G. Bünzli, G. Hopfgartner, *Inorg. Chem.* **2000**, *39*, 5059–5073; c) T. Lathion, L. Guénée, C. Besnard, A. Bousseksou, C. Piguat, *Chem. – Eur. J.* **2018**, *24*, 16873–16888; d) T. Lathion, A. Fürstenberg, C. Besnard, A. Hauser, A. Bousseksou, C. Piguat, *Inorg. Chem.* **2020**, *59*, 1091–1103.
- [29] a) F. Tuna, M. R. Lees, G. J. Clarkson, M. J. Hannon, *Chem. – Eur. J.* **2004**, *10*, 5737–5750; b) Y. Garcia, C. M. Grunert, S. Reiman, O. van Campenhoudt, P. Güttlich, *Eur. J. Inorg. Chem.* **2006**, 3333–3339.
- [30] Other recent SCO [3+3] helicates of bis-bidentate Schiff base ligands: a) N. Struch, F. Topić, G. Schnakenburg, K. Rissanen, A. Lützen, *Inorg. Chem.* **2018**, *57*, 241–250; b) A. R. Craze, M. M. Bhadbhade, Y. Komatsumaru, C. E. Marjo, S. Hayami, F. Li, *Inorg. Chem.* **2020**, *59*, 1274–1283; c) A. R. Craze, H. Zenno, M. C. Pfrunder, J. C. McMurtrie, S. Hayami, J. K. Clegg, F. Li, *Inorg. Chem.* **2021**, *60*, 6731–6738; d) S. Athira, D. J. Mondal, S. Shome, B. Dey, S. Konar, *Dalton Trans.* **2022**, *51*, 16706–16713.
- [31] S. Singh, S. Brooker, *Chem. Sci.* **2021**, *12*, 10919–10929.
- [32] a) H. Hagiwara, T. Tanaka, S. Hora, *Dalton Trans.* **2016**, *45*, 17132–17140; b) S. Hora, H. Hagiwara, *Inorganics* **2017**, *5*, 49.
- [33] M. A. Halcrow, *Coord. Chem. Rev.* **2009**, *253*, 2493–2514
- [34] L. J. Kershaw Cook, R. Mohammed, G. Sherborne, T. D. Roberts, S. Alvarez, M. A. Halcrow, *Coord. Chem. Rev.* **2015**, *289–290*, 2–12.
- [35] M. A. Halcrow, I. Capel Berdiell, C. M. Pask, R. Kulmaczewski, *Inorg. Chem.* **2019**, *58*, 9811–9821.
- [36] Selected recent reports of [Fe(1-bpp)₂]²⁺ SCO complexes. a) K. Senthil Kumar, N. Del Giudice, B. Heinrich, L. Douce, M. Ruben, *Dalton Trans.* **2020**, *49*, 14258–14267; b) R. Kulmaczewski, F. Bamiduro, O. Cespedes, M. A. Halcrow, *Chem. – Eur. J.* **2021**, *27*, 2082–2092; c) I. Galadzhun, R. Kulmaczewski, N. Shahid, O. Cespedes, M. J. Howard, M. A. Halcrow, *Chem. Commun.* **2021**, *57*, 4039–4042; d) I. Capel Berdiell, R. Kulmaczewski, N. Shahid, O. Cespedes, M. A. Halcrow, *Chem. Commun.* **2021**, *57*, 6566–6569; e) M. Attwood, H. Akutsu, L. Martin, T. J. Blundell, P. Le Maguere, S. S. Turner, *Dalton Trans.* **2021**, *50*, 11843–11851; f) Q. Yang, Y.-S. Meng, T. Liu, J. Tang, *Dalton Trans.* **2022**, *51*, 602–607; g) N. Suryadevara, A. Mizuno, L. Spieker, S. Salamon, S. Sleziona, A. Maas, E. Pollmann, B. Heinrich, M. Schleberger, H. Wende, S. K. Kuppasamy, M. Ruben, *Chem. – Eur. J.* **2022**, *28*, e202103853; h) R. Kulmaczewski, L. J. Kershaw Cook, C. M. Pask, O. Cespedes, M. A. Halcrow, *Cryst. Growth Des.* **2022**, *22*, 1960–1971.
- [37] G. A. Craig, O. Roubeau, G. Aromí, *Coord. Chem. Rev.* **2014**, *269*, 13–31.
- [38] Selected recent reports of [Fe(3-bpp)₂]²⁺ SCO complexes. a) I. Nikovskiy, A. Polezhaev, V. Novikov, D. Aleshin, A. Pavlov, E. Saffulina, R. Aysin, P. Dorovatovskii, L. Nodaraki, F. Tuna, Yu. Nelyubina, *Chem. – Eur. J.* **2020**, *26*, 5629–5638; b) D. Yu. Aleshin, I. Nikovskiy, V. V. Novikov, A. V. Polezhaev, E. K. Melnikova, Yu. V. Nelyubina, *ACS Omega* **2021**, *6*, 33111–33121; c) V. Jornet-Mollá, C. Giménez-Saiz, D. S. Yufit, J. A. K. Howard, F. M. Romero, *Chem. – Eur. J.* **2021**, *27*, 740–750; d) V. Jornet-Mollá, C. Giménez-Saiz, L. Cañadillas-Delgado, D. S. Yufit, J. A. K. Howard, F. M. Romero, *Chem. Sci.* **2021**, *12*, 1038–1053; e) Ö. Üngör, E. S. Choi, M. Shatruk, *Chem. Sci.* **2021**, *12*, 10765–10779; f) A. Djemel, O. Stefanczyk, C. Desplanches, K. Kumar, R. Delimi, F. Benaceur, S.

- Ohkoshi, G. Chastanet, *Inorg. Chem. Front.* **2021**, *8*, 3210–3221; g) L. T. Birchall, G. Truccolo, L. Jackson, H. J. Shepherd, *Chem. Sci.* **2022**, *13*, 3176–3186.
- [39] C. Bartual-Murgui, C. Codina, O. Roubeau, G. Aromí, *Chem. – Eur. J.* **2016**, *22*, 12767–12776.
- [40] C. Bartual-Murgui, S. Vela, M. Darawsheh, R. Diego, S. J. Teat, O. Roubeau, G. Aromí, *Inorg. Chem. Front.* **2017**, *4*, 1374–1383.
- [41] a) C. Bartual-Murgui, S. Vela, O. Roubeau, G. Aromí, *Dalton Trans.* **2016**, *45*, 14058–14062; b) C. Bartual-Murgui, C. Pérez-Padilla, S. J. Teat, O. Roubeau, G. Aromí, *Inorg. Chem.* **2020**, *59*, 12132–12142.
- [42] Other linear helicate complexes formed from multitopic bpp derivatives: a) A. T. Baker, D. C. Craig, G. A. Dong, *Inorg. Chem.* **1996**, *35*, 1091–1092; b) S. P. Argent, H. Adams, L. P. Harding, T. Riis-Johannessen, J. C. Jeffery, M. D. Ward, *New J. Chem.* **2005**, *29*, 904–911; c) Q.-D. Shu, S.-N. Kong, L. Feng, M. H. Shu, *Polyhedron* **2016**, *109*, 47–52.
- [43] Tetrametallic [2×2] grid complexes supported by multitopic bpp derivatives: a) J. S. Costa, G. A. Craig, L. A. Barrios, O. Roubeau, E. Ruiz, S. Gómez-Coca, S. J. Teat, G. Aromí, *Chem. – Eur. J.* **2011**, *17*, 4960–4963; b) J. Tong, S. Demeshko, M. John, S. Dechert, F. Meyer, *Inorg. Chem.* **2016**, *55*, 4362–4372.
- [44] Other high-nuclearity metal/organic assemblies formed from multitopic bpp derivatives: a) G. A. Dong, A. T. Baker, D. C. Craig, *Inorg. Chim. Acta* **1995**, *231*, 241–244; b) T. Shiga, T. Matsumoto, M. Noguchi, T. Onuki, N. Hoshino, G. N. Newton, M. Nakano, H. Oshio, *Chem. – Asian J.* **2009**, *4*, 1660–1663; c) G. N. Newton, T. Onuki, T. Shiga, M. Noguchi, T. Matsumoto, J. S. Mathieson, M. Nihei, M. Nakano, L. Cronin, H. Oshio, *Angew. Chem. Int. Ed.* **2011**, *50*, 4844–4848; *Angew. Chem.* **2011**, *123*, 4946–4950; d) G. A. Craig, O. Roubeau, J. Ribas-Ariño, S. J. Teat, G. Aromí, *Polyhedron* **2013**, *52*, 1369–1374; e) H. Sato, L. Miya, K. Mitsumoto, T. Matsumoto, T. Shiga, G. N. Newton, H. Oshio, *Inorg. Chem.* **2013**, *52*, 9714–9716; f) G. A. Craig, M. Schütze, D. Aguilà, D.; O. Roubeau, J. Ribas-Ariño, S. Vela, S. J. Teat, G. Aromí, *Inorg. Chem.* **2014**, *53*, 3290–3297; g) H. Sato, M. Yamaguchi, T. Onuki, M. Noguchi, G. N. Newton, T. Shiga, H. Oshio, *Eur. J. Inorg. Chem.* **2015**, 2193–2198.
- [45] J. M. Holland, J. A. McAllister, C. A. Kilner, M. Thornton-Pett, A. J. Bridgeman, M. A. Halcrow, *J. Chem. Soc. Dalton Trans.* **2002**, 548–554.
- [46] A [Fe(bpp)₂]²⁺ derivative with local D_{2d} symmetry exhibits $\phi = 180$ and $\theta = 90^\circ$. Low-spin molecules generally show small deviations from these idealized values, but high-spin [Fe(bpp)₂]²⁺ complexes with $150 \leq \phi \leq 180^\circ$ and $60 \leq \theta \leq 90^\circ$ have been reported (Figure 2).^[33–35,37]
- [47] L. J. Kershaw Cook, F. L. Thorp-Greenwood, T. P. Comyn, O. Cespedes, G. Chastanet, M. A. Halcrow, *Inorg. Chem.* **2015**, *54*, 6319–6330.
- [48] S. Vela, J. J. Novoa, J. Ribas-Arino, *Phys. Chem. Chem. Phys.* **2014**, *16*, 27012–27024.
- [49] V_{OH} is the volume of the octahedron defined by the FeN₆ coordination sphere.^[73] Σ is a general measure of the deviation of a metal ion from an ideal octahedral geometry, while θ more specifically indicates its distortion toward a trigonal-prismatic structure.^[73,74] Σ and θ are usually much larger in the high-spin state than in the low-spin state; a perfectly octahedral complex gives $\Sigma = \theta = 0$. Typical values for these parameters in high- and low-spin [Fe(bpp)₂]²⁺ derivatives are given in refs [33, 34 and 56].
- [50] a) G. Ritter, E. König, W. Irlner, H. A. Goodwin, *Inorg. Chem.* **1978**, *17*, 224–228; b) J.-F. Létard, S. Asthana, H. J. Shepherd, P. Guionneau, A. E. Goeta, N. Suemura, R. Ishikawa, S. Kaizaki, *Chem. – Eur. J.* **2012**, *18*, 5924–5934; c) N. Paradis, G. Chastanet, J.-F. Létard, *Eur. J. Inorg. Chem.* **2012**, 3618–3624; d) N. Paradis, G. Chastanet, T. Palamarciuc, P. Rosa, F. Varret, K. Boukheddaden, J.-F. Létard, *J. Phys. Chem. C* **2015**, *119*, 20039–20050; e) Y. S. Ye, X. Q. Chen, Y. D. Cai, B. Fei, P. Dechambenoit, M. Rouzières, C. Mathonière, R. Clérac, X. Bao, *Angew. Chem. Int. Ed.* **2019**, *58*, 18888–18891; *Angew. Chem.* **2019**, *131*, 19064–19067.
- [51] a) V. A. Money, C. Carbonera, J. Elhaik, M. A. Halcrow, J. A. K. Howard, J.-F. Létard, *Chem. – Eur. J.* **2007**, *13*, 5503–5514; b) R. Kulmaczewski, E. Trzop, L. J. Kershaw Cook, E. Collet, G. Chastanet, M. A. Halcrow, *Chem. Commun.* **2017**, 13268–13271.
- [52] a) L. J. Kershaw Cook, J. Fisher, L. P. Harding, M. A. Halcrow, *Dalton Trans.* **2015**, *44*, 9417–9425; b) I. Šalitroš, R. Herchel, O. Fuhr, R. González-Prieto, M. Ruben, *Inorg. Chem.* **2019**, *58*, 4310–4319.
- [53] N. Suryadevara, A. Pausch, E. Moreno-Pineda, A. Mizuno, J. Bürck, A. Baksi, T. Hochdörffer, I. Šalitroš, A. S. Ulrich, M. M. Kappes, V. Schünemann, W. Klopfer, M. Ruben, *Chem. – Eur. J.* **2021**, *27*, 15171–15179.
- [54] The calculations were performed using SPARTAN¹⁸, which does not include a solvent correction for transition metals. Hence, all the calculations in this study are the gas phase.
- [55] Figures of the DFT- and molecular mechanics-minimized molecules; Tables of their energies, atomic coordinates and metric parameters; and representative frontier orbital plots for the iron(II) and chromium(0) helicate complexes are given in the Supporting Information.
- [56] I. Capel Berdiell, R. Kulmaczewski, M. A. Halcrow, *Inorg. Chem.* **2017**, *56*, 8817–8828.
- [57] R. Kulmaczewski, M. J. Howard, M. A. Halcrow, *Dalton Trans.* **2021**, *50*, 3464–3467.
- [58] a) N. Shahid, K. E. Burrows, C. M. Pask, O. Cespedes, M. J. Howard, P. C. McGowan, M. A. Halcrow, *Inorg. Chem.* **2021**, *60*, 14336–14348; b) N. Shahid, K. E. Burrows, C. M. Pask, O. Cespedes, M. J. Howard, P. C. McGowan, M. A. Halcrow, *Dalton Trans.* **2022**, *51*, 4262–4274 and **2022**, *51*, 6486 (correction).
- [59] I. Capel Berdiell, D. J. Davies, J. Woodworth, R. Kulmaczewski, O. Cespedes, M. A. Halcrow, *Inorg. Chem.* **2021**, *60*, 14988–15000.
- [60] a) S. Zein, S. A. Borshch, P. Fleurat-Lessard, M. E. Casida, H. Chermette, *J. Chem. Phys.* **2007**, *126*, 014105; b) B. J. Houghton, R. J. Deeth, *Eur. J. Inorg. Chem.* **2014**, 4573–4580; c) S. R. Mortensen, K. P. Kepp, *J. Phys. Chem. A* **2015**, *119*, 4041–4050; d) O. S. Siig, K. P. Kepp, *J. Phys. Chem. A* **2018**, *122*, 4208–4217.
- [61] The minimized S = 2 Cr₂ helicates consistently contain one low-spin Cr(0) ion and one high-spin Cr(II) center, but the S = 4 minimizations are more complicated. One of their Cr atoms always resembles the Cr(II) ion in the mixed-spin molecules, but the structure of the other Cr atom is more variable. In some cases the second Cr atom also has a distorted Cr(II)-like geometry, while in others it has a more regular pattern of Cr–N bond lengths. This is discussed further in the Supporting Information.
- [62] Stepwise SCO has been observed in other types of dinuclear iron(II) complex, although this can proceed via a mixed high-spin/low-spin phase rather than a mixed-spin intermediate species: a) K. Nakano, S. Kawata, K. Yoneda, A. Fuyuhiro, T. Yagi, S. Nasu, S. Morimoto, S. Kaizaki, *Chem. Commun.* **2004**, 2892–2893; b) V. Ksenofontov, A. B. Gaspar, V. Niel, S. Reiman, J. A. Real, P. Gütllich, *Chem. – Eur. J.* **2004**, *10*, 1291–1298; c) J. J. M. Amore, C. J. Kepert, J. D. Cashion, B. Moubaraki, S. M. Neville, K. S. Murray, *Chem. – Eur. J.* **2006**, *12*, 8220–8227; d) A. B. Gaspar, V. Ksenofontov, S. Reiman, P. Gütllich, A. L. Thompson, A. E. Goeta, M. C. Muñoz, J. A. Real, *Chem. – Eur. J.* **2006**, *12*, 9289–9298; e) G. S. Matouzenko, E. Jeanneau, A. Yu. Verat, Y. de Gaetano, *Eur. J. Inorg. Chem.* **2012**, 969–977; f) J. E. Clements, P. R. Airey, F. Ragon, V. Shang, C. J. Kepert, S. M. Neville, *Inorg. Chem.* **2018**, *57*, 14930–14938; g) F. Färmeyer, L. M. Carrella, V. Ksenofontov, A. Möller, E. Rentschler, *Inorg. Chem.* **2020**, *59*, 2843–2852.
- [63] a) S. Zein, S. A. Borshch, *J. Am. Chem. Soc.* **2005**, *127*, 16197–16201; b) A. Yu. Verat, N. Ould-Moussa, E. Jeanneau, B. Le Guennic, A. Bousseksou, S. A. Borshch, G. S. Matouzenko, *Chem. – Eur. J.* **2009**, *15*, 10070–10082; c) C. J. Schneider, J. D. Cashion, N. F. Chilton, C. Etrillard, M. Fuentealba, J. A. K. Howard, J.-F. Létard, C. Milsmann, B. Moubaraki, H. A. Sparkes, S. R. Batten, K. S. Murray, *Eur. J. Inorg. Chem.* **2013**, 850–864; d) Q. M. Phung, A. Domingo, K. Pierloot, *Chem. – Eur. J.* **2018**, *24*, 5183–5190.
- [64] a) E. M. Zueva, E. R. Ryabikh, A. M. Kuznetsov, S. A. Borshch, *Inorg. Chem.* **2011**, *50*, 1905–1913; b) E. M. Zueva, E. R. Ryabikh, S. A. Borshch, *Inorg. Chem.* **2011**, *50*, 11143–11151; c) S. A. Borshch, E. M. Zueva, *Eur. J. Inorg. Chem.* **2013**, 1009–1014.
- [65] Periodic DFT+U calculations on dinuclear SCO complexes have recently been reported, which account for intermolecular interactions in the solid state and should give more accurate spin-state energies: a) A. Chakraborty, A. Chakraborty, S. Ghosh, I. Dasgupta, *J. Phys.: Condens. Matter* **2020**, *32*, 165802; b) F.-L. Yang, W.-H. Wu, Y.-Q. Wang, X. Chen, B.-B. Liang, H.-L. Mi, G.-L. Zhang, X.-Y. Chen, Y. Shi, *Cryst. Growth Des.* **2021**, *21*, 6671–6683.
- [66] C. J. O'Connor, *Prog. Inorg. Chem.* **2007**, *29*, 203–283.

- [67] *ORIGINPro* 2020, OriginLab Corporation, Northampton, MA, USA.
- [68] *Bruker Compass Data Analysis* v. 4.3, Bruker Daltonics Inc, Billerica, MA 01821, USA, **2014**.
- [69] *Spartan'18*; Wavefunction Inc.: Irvine, CA, USA, **2016**.
- [70] G. M. Sheldrick, *Acta Cryst. Sect. C: Struct. Chem.* **2015**, *71*, 3–8.
- [71] L. J. Barbour, *J. Appl. Cryst.* **2020**, *53*, 1141–1146.
- [72] O. V. Dolomanov, L. J. Bourhis, R. J. Gildea, J. A. K. Howard, H. Puschmann, *J. Appl. Cryst.* **2009**, *42*, 339–341.
- [73] P. Guionneau, M. Marchivie, G. Bravic, J.-F. Létard, D. Chasseau, *Top. Curr. Chem.* **2004**, *234*, 97–128.
- [74] J. K. McCusker, A. L. Rheingold, D. N. Hendrickson, *Inorg. Chem.* **1996**, *35*, 2100–2112.